A&A 419, 501–516 (2004)
DOI: 10.1051/0004-6361:20040963

Astronomy & Astrophysics

Warm dust and aromatic bands as quantitative probes of star-formation activity⋆

N. M. Förster Schreiber[1], H. Roussel[2], M. Sauvage[3], and V. Charmandaris[4,5]

[1] Leiden Observatory, Leiden University, Postbus 9513, RA Leiden, The Netherlands
e-mail: forster@strw.leidenuniv.nl
[2] California Institute of Technology, Pasadena, CA 91125, USA
[3] CEA/DSM/DAPNIA/Service d'Astrophysique, CE Saclay, 91191 Gif-sur-Yvette Cedex, France
e-mail: msauvage@cea.fr
[4] Cornell University, Astronomy Department, Ithaca, NY 14853, USA
[5] Chercheur associé, Observatoire de Paris, LERMA, 75014 Paris, France
e-mail: vassilis@astro.cornell.edu

Received 2 January 2004 / Accepted 23 February 2004

Abstract. We combine samples of spiral galaxies and starburst systems observed with ISOCAM on board ISO to investigate the reliability of mid-infrared dust emission as a quantitative tracer of star formation activity. The total sample covers very diverse galactic environments and probes a much wider dynamic range in star formation rate density than previous similar studies. We find that both the monochromatic 15 μm continuum and the 5−8.5 μm emission constitute excellent indicators of the star formation rate as quantified by the Lyman continuum luminosity $L_{\rm Lyc}$, within specified validity limits which are different for the two tracers. Normalized to projected surface area, the 15 μm continuum luminosity $\Sigma_{15\,\mu{\rm m,ct}}$ is directly proportional to $\Sigma_{\rm Lyc}$ over several orders of magnitude. Two regimes are distinguished from the relative offsets in the observed relationship: the proportionality factor increases by a factor of ≈5 between quiescent disks in spiral galaxies, and moderate to extreme star-forming environments in circumnuclear regions of spirals and in starburst systems. The transition occurs near $\Sigma_{\rm Lyc} \sim 10^2\ L_\odot\,{\rm pc}^{-2}$ and is interpreted as due to very small dust grains starting to dominate the emission at 15 μm over aromatic species above this threshold. The 5−8.5 μm luminosity per unit projected area is also directly proportional to the Lyman continuum luminosity, with a single conversion factor from the most quiescent objects included in the sample up to $\Sigma_{\rm Lyc} \sim 10^4\ L_\odot\,{\rm pc}^{-2}$, where the relationship then flattens. The turnover is attributed to depletion of aromatic band carriers in the harsher conditions prevailing in extreme starburst environments. The observed relationships provide empirical calibrations useful for estimating star formation rates from mid-infrared observations, much less affected by extinction than optical and near-infrared tracers in deeply embedded H II regions and obscured starbursts, as well as for theoretical predictions from evolutionary synthesis models.

Key words. galaxies: ISM – galaxies: starburst – galaxies: stellar content – infrared: galaxies – infrared: ISM

1. Introduction

Star formation is a fundamental process of galaxy formation and evolution. Estimates of the star formation rate (SFR) in galaxies at all redshifts are key indicators of the efficiency and mechanical feedback effects of star formation activity, of the chemical evolution of the interstellar and intergalactic medium, and, ultimately, of the cosmic star formation history.

Commonly used probes of the SFR include photospheric emission from hot stars in the ultraviolet, nebular H and He recombination lines as well as fine-structure lines arising in H II regions from optical to radio wavelengths, and the total infrared luminosity ($\lambda = 8-1000\,\mu$m), the bulk of which is due to heated dust reprocessing the interstellar radiation field (see, e.g., the review by Kennicutt 1998). However, ultraviolet, optical, and even near-infrared diagnostics are subject to potentially large uncertainties because of extinction in deeply embedded young star-forming sites and in nuclear regions of galaxies. Nebular lines may be difficult to measure when intrinsically weak or superposed over a strong continuum. While dust emission suffers very little from extinction effects and is usually strong in star-forming environments, the total infrared luminosity is difficult to evaluate because it is generally derived from observations in a few wavelength intervals which do not constrain the spectral energy distribution accurately. Moreover, a cirrus-like component unrelated to star-forming regions can

Send offprint requests to: H. Roussel,
e-mail: hroussel@irastro.caltech.edu

⋆ Based on observations with ISO, an ESA project with instruments funded by ESA member states (especially the PI countries: France, Germany, The Netherlands, and the UK), and with participation of ISAS and NASA.

contribute substantially to the far-infrared output of galaxies (Helou 1986; Sauvage & Thuan 1992).

Mid-infrared emission (MIR, $\lambda = 5-20\,\mu$m) provides an alternative probe of star formation activity. The "classical" spectrum of star-forming sources exhibits broad emission features often referred to as "unidentified infrared bands" (UIBs) and of which the most prominent dominate the $6-13\,\mu$m range, and a continuum rising towards long wavelengths at $\lambda \gtrsim 11\,\mu$m (see the reviews by Geballe 1997; Tokunaga 1997; Cesarsky & Sauvage 1999; Genzel & Cesarsky 2000). Various carbonaceous materials have been proposed to carry the UIBs, including the popular polycyclic aromatic hydrocarbons (PAHs; e.g. Léger & Puget 1984) that we adopt hereafter. Peeters et al. (2002) have analysed their shape and relative amplitude variations in different classes of Galactic objects. The continuum emission is generally attributed to very small dust grains (VSGs; e.g. Désert et al. 1990) about which little is known. Superposed on these PAH and VSG components, H recombination lines and fine-structure lines of various metals originating in H II and photodissociation regions are observed as well (e.g. Sturm et al. 2000). These lines may however not always be measurable because of their weakness or of insufficient spectral resolution.

Numerous past studies have established that PAH and $\lambda \gtrsim 11\,\mu$m continuum emission trace well star-forming regions but their usefulness as *quantitative* diagnostics is still debated. Complications arise from the different nature of the emitting particles and by their being out of thermal equilibrium under most radiation field conditions, undergoing large temperature fluctuations of several 100 K (e.g. Greenberg & Hong 1985; Draine & Anderson 1985; Puget & Léger 1989). In addition, although both species are predominantly heated by energetic radiation, PAHs can also be excited by softer optical and near-ultraviolet photons as indicated by their detection in the diffuse interstellar medium, in regions of insufficient far-ultraviolet energy density to account for their heating (e.g. Sellgren et al. 1990; Mattila et al. 1996; Uchida et al. 1998, 2000; Li & Draine 2002). Furthermore, empirical evidence indicates that the $\lambda \gtrsim 11\,\mu$m emission is produced by a mixture of dust particles akin to PAHs (or at least whose flux variations follow well those of PAHs) and of VSGs (e.g. Hony et al. 2001; Roussel et al. 2001b). The first component is best seen in quiescent environments such as disks of spiral galaxies while the second becomes prominent in active star formation sites. It is not yet clear how their combined emission varies over a large dynamic range in star formation intensity.

On the other hand, spatially resolved studies of Galactic and Magellanic Clouds H II regions have revealed that both the PAH features and the VSG continuum are produced in the vicinity of massive stars, the former arising in photodissociation regions (PDRs) at the interface between ionized and molecular gas and the latter peaking closer to the ionizing stars (e.g. Geballe 1997; Tokunaga 1997; Verstraete et al. 1996; Crété et al. 1999; Contursi et al. 2000). MIR imaging of external galaxies has shown that bright emission from both components is closely associated with active star-forming sites on large scales as well (e.g. Mirabel et al. 1998; Mattila et al. 1999; Roussel et al. 2001c; Förster Schreiber et al. 2003). A strong coupling with the SFR may thus exist and has been demonstrated for disks of spiral galaxies by Roussel et al. (2001c). Specifically, these authors found that the broadband $5-8.5\,\mu$m and $12-18\,\mu$m fluxes vary linearly with the Hα line flux in the disks of 44 spirals. Förster Schreiber et al. (2003) also found a direct proportionality between the monochromatic 15 μm continuum ($\Delta\lambda = 0.4\,\mu$m) and the [Ar II] 6.99 μm line emission in the nearby starbursts M 82, NGC 253, and NGC 1808, down to spatial scales of ∼100 pc.

In this paper, we pursue the work of Roussel et al. (2001c) and Förster Schreiber et al. (2003) by combining samples of spiral and starburst galaxies observed with the ISOCAM instrument (Cesarsky et al. 1996) on board the Infrared Satellite Observatory (ISO; Kessler et al. 1996). The merged sample covers diverse environments ranging from quiescent galactic disks to infrared-luminous merging systems. This allows us to extend the investigation to higher activity levels and to test whether previous results restricted to specific environments can be generalized into more universal relationships. We derive the dependence of the PAH-dominated $5-8.5\,\mu$m emission and the VSG-probing monochromatic $15\,\mu$m continuum on the production rate of Lyman continuum photons $Q_{\rm Lyc}$ quantifying the SFR. The resulting empirical calibrations provide useful tools in MIR studies of star-forming galaxies as well as constraints for models predicting the dust emission of such systems.

The paper is organized as follows. Section 2 presents the galaxy sample. Section 3 describes the MIR indicators and the SFR estimates obtained from more classical diagnostics. Section 4 discusses the derived calibrations and Sect. 5 summarizes the results.

2. Galaxy sample

We drew our sample from separate studies published by us and from the ISO archive. All sources were observed with ISOCAM either with the broadband filters *LW*2 centered at 7 μm ($5-8.5\,\mu$m) and *LW*3 centered at 15 μm ($12-18\,\mu$m) or with the continuously variable filter (CVF) covering the $5-17\,\mu$m range at a resolution of $R \equiv \lambda/\Delta\lambda \sim 40$. Ten galaxies were observed in both broadband photometric mode and spectrophotometric mode. We used this subset to assess the photometric consistency and to derive conversion factors between measurements obtained through the ISOCAM filters and from the CVF spectra (Sect. 3.1). Details of the observations are given in the relevant references (Table 1). To our knowledge, the ISOCAM data of IC 342 have not been published anywhere else; they are briefly presented in Appendix B.

The sample can be divided in four parts, in order of increasing star formation activity:

- disks of spiral galaxies, which form stars in a quiescent fashion and for which the relationship between the MIR emission and the SFR, as derived from Hα line measurements, was discussed by Roussel et al. (2001c);
- the more active circumnuclear regions of a subsample of the same galaxies, for which it was possible to estimate an extinction-free SFR from a combination of near-infrared H recombination lines and Hα;

Table 1. Sample of galaxies and ISOCAM observations: circumnuclear regions of spiral galaxies and starbursts.

Source	Distance [a] (Mpc)	Morph. type [b]	Nuclear type [c]	L_{IR} [d] ($L_\odot$)	Observations [e]	Project [f]	Reference [g]
Circumnuclear regions of spiral galaxies							
NGC 986	23.2	SBab	H II	4.6×10^{10}	LW	Sf_glx	1, 3
NGC 1097	14.5	SBb	Liner/Sy	3.8×10^{10}	LW + CVF	CAMbarre	2
NGC 1365	16.9	SBb	Sy	8.7×10^{10}	LW + CVF	CAMspir	2
NGC 4102	17.0	SABb	H II	4.2×10^{10}	LW	Sf_glx	1, 3
NGC 4293	17.0	SB0/a	Liner	4.7×10^{9}	LW	Virgo	4, 2
NGC 4691	22.5	SB0/a	H II	2.4×10^{10}	LW	CAMbarre	2
NGC 5194 (M 51)	7.7	SAbc, int.	Sy	2.4×10^{10}	LW + CVF	CAMspir	5, 2
NGC 5236 (M 83)	4.7	SABc	H II	1.9×10^{10}	LW + CVF	CAMspir	2
NGC 6946	5.5	SABcd	H II	1.4×10^{10}	LW + CVF	Sf_glx, Zzcvfcam	6, 2
NGC 7552	19.5	SBab	H II	8.6×10^{10}	LW	CAMbarre	2
NGC 7771†	57.2	SBa, int.	H II	2.1×10^{11}	LW	Sf_glx	1, 3
Starburst galaxies							
NGC 253	2.5	SABc	H II	1.8×10^{10}	CVF	CAMACTIV	7
NGC 520	27.8	Pec, merger	H II	6.5×10^{10}	LW + CVF	CAMACTIV	8
NGC 1808	10.8	RSABa, int.	H II	3.8×10^{10}	LW + CVF	CAMACTIV	7
NGC 3034 (M 82)	3.3	I0, int.	H II	4.8×10^{10}	CVF	CAMACTIV	7
IC 342	3.3	SAB(rs)cd	H II	3.3×10^{9}	CVF	IMSP_SBG	
LIRGs/ULIRGs							
NGC 3256	37.4	Pec, merger	H II	4.0×10^{11}	CVF	CAMACTIV	8, 10
NGC 6240	97.2	I0:pec, merger	Liner	6.0×10^{11}	LW + CVF	CAMACTIV	8, 10
IRAS 23128-5919	180	merger	H II	9.4×10^{11}	LW + CVF	CAMACTIV	9
Arp 220	72.5	S? (Pec), merger	Liner	1.3×10^{12}	LW + CVF	CAMACTIV	8, 10

[a] Distances are from the NGC catalogue (Tully 1988) with the following exceptions: NGC 253: Davidge & Pritchet (1990); M 82: Freedman & Madore (1988); IC 342: Saha et al. (2002); NGC 7771, NGC 6240, and Arp 220: computed from the H I redshifts given in the RC3 catalog (z = 0.014300, 0.024307, and 0.018126, respectively; de Vaucouleurs et al. 1991); IRAS 23128-5919: luminosity distance computed by Charmandaris et al. (2002). All distances assume $H_0 = 75$ km s^{-1} Mpc^{-1} and $q_0 = 0.5$ where relevant.

[b] Morphological types are from the RC3 catalogue (de Vaucouleurs et al. 1991), with additional indications for interacting ("int.") or merging system.

[c] Nuclear types give an indication of the nuclear activity inferred from optical spectra. The types for the normal spiral galaxies are as listed by Roussel et al. (2001b,see their Table 1 for references). For a subset of the starburst systems, references are Kewley et al. (2001, NGC 253, N1808, IRAS 23128-5919), Stanford (1991, NGC 520), Veilleux et al. (1995, NGC 6240), Kim et al. (1998, Arp 220). The types for the remaining starbursts are those listed in the NED database.

[d] Global infrared (8−1000 μm) luminosity computed from the *IRAS* fluxes following Sanders & Mirabel (1996).

[e] Data available from ISOCAM observations and used in our analysis: "*LW*" for data obtained in the broad band filters *LW*2 and *LW*3 (5.0−8.5 μm and 12−18 μm), "CVF" for 5−17 μm spectrophotometric imaging at $R \sim 40$.

[f] Observing program. Sf_glx: P.I. G. Helou; CAMbarre: P.I. C. Bonoli; CAMspir: P.I. L. Vigroux; Virgo: P.I. J. Lequeux; Zzcvfcam: P.I. D. Cesarsky; CAMACTIV: P.I. Mirabel; IMSP_SBG: P.I. R. Maiolino.

[g] References for initial publication of the ISOCAM data: (1) Dale et al. (2000); (2) Roussel et al. (2001a); (3) Roussel et al. (2001b); (4) Boselli et al. (1998); (5) Sauvage et al. (1996); (6) Malhotra et al. (1996); (7) Förster Schreiber et al. (2003); (8) Laurent et al. (2000); (9) Charmandaris et al. (2002); (10) Tran et al. (2001).

† This galaxy also is a LIRG, but about half its total mid-infrared emission arises outside the central regions selected here.

– nearby starburst galaxies, three of which were studied in detail by Förster Schreiber et al. (2001, 2003) in their dust and fine-structure line emission;
– luminous and ultraluminous infrared galaxies (LIRGs and ULIRGs, with $10^{11} < L_{IR} < 10^{12}\ L_\odot$ and $L_{IR} \geq 10^{12}\ L_\odot$, respectively[1]) taken from the samples studied by Laurent et al. (2000), Tran et al. (2001) and Charmandaris et al. (2002).

Most objects are purely star-forming systems; a few harbour an active galactic nucleus (AGN) revealed by optical spectroscopy, which is however known or suspected to contribute but negligibly to the MIR emission, as well as to the hydrogen recombination lines within our photometric apertures, which are very large with respect to the angular size of the nucleus. Detailed notes and discussion of individual cases are given in Appendix A. The LIRGs and ULIRGs will also be referred to as starbursts throughout the paper. Table 1 lists the non-disk objects (circumnuclear regions of spirals and starburst

[1] $L_{IR} \equiv L_{8-1000\,\mu m}$ is the total infrared luminosity computed from *IRAS* fluxes following the prescription of Sanders & Mirabel (1996).

systems). The table gives some general properties, the observation mode, and the original observing program to which they belong. Similar details for the spiral disk sample are given by Roussel et al. (2001a,b).

In spiral galaxies, the low brightness disks and central regions are distinguished by different ratios of flux density in the *LW*3 and *LW*2 filters, or $f_{12-18\,\mu m}/f_{5-8.5\,\mu m}$ color: the disks typically have ratios of ≈1 while the circumnuclear regions usually exhibit a color excess signaling more active star formation[2] (e.g. Dale et al. 2000; Roussel et al. 2001b). We adopted the measurements for disks reported by Roussel et al. (2001c). Briefly, these were obtained from the integrated MIR and Hα fluxes by subtracting the contribution from a core region and accounting for flux dilution effects of the ISOCAM point spread function (PSF; see Roussel et al. 2001a). The size of the excluded area was dictated by the Hα data existing in the literature (fluxes in given apertures, or maps). In the few cases where the Hα aperture is smaller than D_{CNR}, the size of the circumnuclear regions fitted on MIR brightness profiles, it was ensured that the resulting disk $f_{12-18\,\mu m}/f_{5-8.5\,\mu m}$ color was close to unity.

Altogether, the sample covers more than five orders of magnitude in Lyman continuum photon flux density Σ_{Lyc} (Sect. 4). The latter implies five orders of magnitude in quasi-instantaneous SFR surface density, assuming that the same stellar initial mass function applies to all objects (e.g. Kennicutt 1998). Our sample is admittedly not complete in any sense and is restricted to near-solar metallicities. For our purposes, it should however provide a sufficiently representative ensemble since the primary samples were constructed with different criteria and aims. Since star-forming systems, both Galactic and extragalactic, have remarkably similar MIR spectral energy distributions (SED) in terms of broad features and continua, we are confident that we are not introducing any bias by selecting particular galaxies. The sample was only shaped by the availability of adequate data. Further details including notes on individual sources are given in Appendix A.

3. Star formation diagnostics

Tables 2 and 3 report the data for circumnuclear regions of spirals and starburst systems that we used in our analysis. The data for spiral disks are described by Roussel et al. (2001c). We reduced and analysed the MIR maps and spectra of the whole sample in a homogeneous way.

3.1. Mid-infrared 5−8.5 μm and 15 μm emission

The shape of the 5−11 μm SED is observed to be nearly invariant in star-forming galaxies and in a variety of Galactic sources while at $\lambda \gtrsim 11\,\mu$m, the substantial drop in the most quiescent galaxies, with contributions by minor aromatic features, contrasts with the increasingly strong and steep continuum of VSGs in more active sources (see Tielens 1999 for a review; see also e.g. Boulanger et al. 1998; Helou et al. 2000; Uchida et al. 2000; Laurent et al. 2000; Sturm et al. 2000; Roussel et al. 2001c; Förster Schreiber et al. 2003). In ULIRGS, extinction effects can be large enough to distort the shape of the PAH complexes especially by the suppression of the 8.6 μm feature (e.g. Rigopoulou et al. 1999). PAH bands are generally very weak or absent in spectra of pure H II regions and AGNs, a fact usually attributed to the destruction of band carriers in hard and intense radiation fields (e.g. Rigopoulou et al. 1999; Laurent et al. 2000, and references therein).

We focussed on two bandpasses sampling as independently as possible the PAH and VSG emission. The *LW*2 band (5−8.5 μm) encompasses the prominent 6.2, 7.7, 8.6 μm PAH complex where the underlying continuum emission is generally weak in environments devoid of non-stellar activity (e.g. Rigopoulou et al. 1999; Laurent et al. 2000; Lu et al. 2003). To probe the VSG emission, we preferred to define a narrow interval measuring the monochromatic flux at 15 μm rather than use broadband measurements through the *LW*3 filter. The *LW*3 bandpass includes the strong 12.7 μm PAH as well as minor features at 13.55, 14.25, and 15.7 μm that probably dominate the SED at low star formation levels (e.g. Sturm et al. 2000; Hony et al. 2001; Roussel et al. 2001c). We defined the 15 μm narrow band as a top-hat profile filter with unit transmission between 14.8 and 15.2 μm, maximizing the VSG contribution by avoiding known PAH features and other possible emission lines. We note that line emission is not expected to contribute significantly to *LW*2 and *LW*3 measurements. For instance, spectra of the ISO Short Wavelength Spectrometer (SWS; de Graauw et al. 1996) at $R \sim 1000$ show that the strongest lines falling within the *LW*2 and *LW*3 bandpasses for M 82 and NGC 253 are [Ar II] 6.99 μm, [Ne II] 12.81 μm, and [Ne III] 15.56 μm (Sturm et al. 2000; Förster Schreiber et al. 2001); we determined that they account for only ≈1% and 3% of the *LW*2 and *LW*3 flux densities, respectively, in both galaxies.

Throughout this paper, we refer to the narrow 15 μm bandpass as "15 μm, ct" and adopt the notations "5−8.5 μm" and "12−18 μm" for *LW*2 and *LW*3. The effective bandwidths are 0.53, 16.18, and 6.75 THz, respectively. Figure 1 shows the corresponding wavelength ranges and transmission profiles on the SWS spectrum of M 82 and on the lower resolution ISOCAM spectrum extracted within the SWS field of view (Förster Schreiber et al. 2001, 2003).

We obtained the $f_{5-8.5\,\mu m}$ flux densities directly from *LW*2 observations when available, or computed them from CVF spectra accounting for the *LW*2 filter transmission profile. Values of $f_{5-8.5\,\mu m}$ derived from *LW*2 and CVF data for all the sources observed in both modes agree within 20%; differences may be attributed in part to possible residuals from ghosts, flat field, and straylight in the CVF data (Biviano et al. 1998a,b; Okumura 2000). Extrapolation of the spectra between ≈16−17 μm and 18 μm is necessary to compare the $f_{12-18\,\mu m}$ fluxes derived from *LW*3 and CVF data; however, for all the galaxies observed in both modes, we find differences of less than 20%, except for NGC 1097 and IRAS 23128-5919, whose CVF data overestimate $f_{12-18\,\mu m}$ by 30% and 41%, respectively. For NGC 1097, this is probably because our correction of the instrument's memory effects is most uncertain at $\lambda \geq 16\,\mu$m. The correction algorithm (Coulais & Abergel 2000)

[2] More generally, such a color excess can also be due to an AGN heating a surrounding nuclear dust torus (e.g. Laurent et al. 2000).

Table 2. Dust emission of circumnuclear regions of spiral galaxies and starbursts.

Source	Region [a]	Area [a]	$f_{5-8.5\,\mu m}$ [b]		$f_{12-18\,\mu m}$ [b]		$f_{15\,\mu m,ct}$ [c]	
			*LW*2	CVF	*LW*3	CVF	*LW*	CVF
	(arcsec)	(pc^2)	(mJy)	(mJy)	(mJy)	(mJy)	(mJy)	(mJy)
Circumnuclear regions of spiral galaxies								
NGC 986	23.6, 18.2	3.27×10^6	324	...	673	...	628	...
NGC 1097	45	7.86×10^6	1280	(1439)	1692	(2200)	...	1641
NGC 1365	40.0, 37.1	7.26×10^6	1972	(1887)	3103	(3451)	...	2940
NGC 4102	32.4, 28.7	4.39×10^6	>571	...	≥1628	...	1673	...
NGC 4293	32.4, 6.0	4.39×10^6	76	...	147	...	134	...
NGC 4691	56.5, 20.4	2.77×10^7	542	...	759	...	582	...
NGC 5194	90	8.87×10^6	1883	(2096)	2021	(2292)	...	1382
NGC 5236	41.2, 38.4	6.01×10^5	(>2753)	3109	(>3589)	5468	...	4369
NGC 6946	35.3, 32.0	5.71×10^5	(>1095)	1503	(>1885)	2174	...	1551
NGC 7552	21.8, 19.9	2.79×10^6	1248	...	≥2316	...	2067	...
NGC 7771	22.4, 20.6	2.56×10^7	314	...	387	...	270	...
Starburst galaxies								
NGC 253	15.9, 14.0	2.27×10^4	...	6588	...	22 755	...	23 913
NGC 520	17.7, 15.3	3.36×10^6	578	(469)	737	(670)	...	560
NGC 1808	25.9, 24.4	1.28×10^6	2645	(2450)	4077	(4448)	...	3426
NGC 3034	30.0, 28.6	1.65×10^5	...	25 812	...	62 366	...	60 000
IC 342	17×17	7.40×10^4	...	1404	...	3527	...	3035
LIRGs/ULIRGs								
NGC 3256	20.0	1.03×10^7	...	1543	...	2960	...	2634
NGC 6240	total (3.)	1.57×10^6	190	(235)	767	(784)	...	801
IRAS 23128-5919	total (4.2)	1.08×10^7	120	(119)	331	(468)	337	(443)
Arp 220	total (2.)	2.11×10^6	191	(196)	765	(869)	...	1170

[a] "Region" refers to the rectangular dimensions or diameter of the photometric aperture; the first value is the aperture, and the second value is the deconvolved size, which was used for the area normalization as given in "Area".

[b] Broad-band flux densities from ISOCAM observations measured either through the *LW*2 and *LW*3 filters or computed from CVF spectra accounting for the filter transmission profiles. Lower limits for *LW* measurements indicate that the nucleus is saturated in the maps; in which case measurements from the CVF spectrum were preferred. Values unused in the present analysis are enclosed in parentheses. From unpublished previous analysis, photometric errors are always dominated by incompletely corrected memory effects in the *LW*2 filter, and in the *LW*3 filter for sources brighter than ≈200−500 mJy. Taking these memory effects into account, it is estimated that average errors are 10% and 20% in *LW*2 and *LW*3, respectively; individual errors for relatively bright galaxies may be as high as 20% and 30%, respectively (Roussel et al. 2001a). In addition, flux calibration uncertainties are of the order of 5% (ISOCAM handbook).

[c] Monochromatic 15 μm continuum flux density derived from *LW*2 and *LW*3 data based on Fig. 2 as explained in Sect. 3.1 or measured directly from CVF spectra. Calibration errors for CVFs are discussed by Biviano et al. (1998a).

requires knowledge of the detector's response during previous exposures. Since CVF spectral scans were performed in order of decreasing wavelength, and the illumination history of the detector prior to our observation is unknown, the spectrum is most affected at long wavelengths. The CVF spectrum of IRAS 23128-5919 has the lowest signal to noise ratio in the sample and is therefore less reliable; we do not use it in what follows.

Six galaxies of our sample were observed only in broad-band photometric mode, so we derived an empirical conversion between $f_{12-18\,\mu m}$ and $f_{15\,\mu m,ct}$ as follows. We relied on the interpretation that the emission in the *LW*2 band is dominated by PAHs, and that the emission in the *LW*3 band is produced mainly both by PAHs (or akin particles) and by VSGs whose flux variations behave differently (see Sect. 1). Under this assumption, $f_{15\,\mu m,ct}$, which is covered by the *LW*3 filter, should also contain contributions from these two species, albeit in different proportions, and we should expect it to be related to the broadband measurements by a simple function. Figure 2 shows the exact values of this function taken by the objects for which $f_{5-8.5\,\mu m}$ and $f_{12-18\,\mu m}$ were measured from *LW*2 and *LW*3 maps, and $f_{15\,\mu m,ct}$ from CVF data. Assuming that the emission covered by the *LW*3 filter is the sum of a component scaling linearly with the emission bands covered by *LW*2 and of a

Table 3. Line fluxes and extinction for circumnuclear regions of spiral galaxies and starbursts.

Source	Aperture [a] (arcsec)	F_λ [b] (10^{-17} W m^{-2})	$F_{\mathrm{H}\alpha}$ [b] (10^{-16} W m^{-2})	A_V [c] (mag)	$\log[Q_\mathrm{Lyc}]$ [d] ($\log[\mathrm{s}^{-1}]$)	References [e]
Circumnuclear regions of spiral galaxies						
NGC 986	23.6, 4 × 4	...	10.2	2.5	53.57	1, 2
NGC 1097	45	...	39.2	1.9	53.55	3, 4
NGC 1365	40.0, 23.5	Brγ: 19.6	35.8, 28.4	2.9	53.95	5, 6
NGC 4102	starburst	Paβ/Brγ: 12.1/6.0	...	7.2	53.55	7
NGC 4293	32.4	Paα: 10.7	0.76	3.8	52.59	8, 9
NGC 4691	56.5, 23.5	Brγ: 3.76	8.59, 7.18	2.4	53.45	10, 11
NGC 5194	90	...	38.6	2.8	53.29	12, 13
NGC 5236	41.2, 23.5	Brγ: 19.6	75.7, 60.6	1.7	52.79	5, 14
NGC 6946	35.3, 23.5	Brγ: 6.1	8.64, 5.80	3.5	52.58	5, 15
NGC 7552	21.8, 14 × 20	Brα: 44.0	30.3, 29.4	2.1	53.75	1, 16
NGC 7771	starburst ring	Paβ/Brγ: 4.0/1.5	...	5.2	53.91	17
Starburst galaxies						
NGC 253	15, 2.4 × 12	Brγ: 91.6	...	8.5	53.13	18
NGC 520	17.7, 6 × 8	Brγ: 1.9	0.52, 0.15	7.4	54.03	19, 20
NGC 1808	20 (total)	Brγ: 31.0	...	4	53.72	21
NGC 3034	30.0	...	...	52 (MIX)†	54.09	22
IC 342	17 × 17, 14 × 20	Brγ: 17.0; Brα: 70.0	...	5.2†	52.48	16, 23
LIRGs/ULIRGs						
NGC 3256	≈20 (total), 3.5″ × 3.5″	Brγ: 15.0	...	5.3	54.54	24, 25
NGC 6240	total	Brγ: 3.1; Paβ: 4.1	...	10.1	54.91	26, 27
IRAS 23128-5919	total, S. nucleus	Paα: 8.0	1.76, 0.93	3.0	54.74	28, 29
Arp 220	total	Brα: 21.0; Brγ: 0.59	...	40.1†	55.33	30, 31

[a] Rectangular dimensions or diameter of the photometric aperture. When two values are given, the first one refers to the primary flux (Hα when present) and the second one to the hydrogen line decrement used to estimate the extinction. The aperture adopted for the size normalization is given in Table 2.

[b] Observed line fluxes used to derive the extinction and/or the ionizing photon flux. When two Hα fluxes are given, they correspond to the two apertures used for photometry and extinction estimation, respectively.

[c] Derived or adopted extinction for a uniform foreground screen (UFS) model except when "MIX" indicates that a homogeneous mixture of dust and sources is assumed.

[d] Derived or adopted intrinsic Lyman continuum photon rate.

[e] References for line fluxes and extinction values (further details are given on the derivation of the data in appendix A): (1) Hα+[N II] map from Hameed & Devereux (1999) (in NED); (2) Extinction from Hβ/Hα of Véron-Cetty & Véron (1986) in 4″ × 4″; (3) Hα+[N II] map graciously provided by T. Storchi-Bergmann (Storchi-Bergman et al. 1996); (4) Average extinction along the starburst ring derived from the data of Kotilainen et al. (2000); (5) Brγ flux from Puxley et al. (1988) in an effective aperture of 23.5″; (6) Hα+[N II] map graciously provided by M. Naslund (Kristen et al. 1997; Lindblad 1999); (7) Brγ and Paβ fluxes from Roussel et al. (2003) in ≈5″ × 5″ (most of starburst enclosed); (8) Paα map from Böker et al. (1999) (in NED); (9) Hα+[N II] map from Koopmann et al. (2001) (in NED); (10) Brγ flux from Puxley et al. (1990) in an effective aperture of 23.5″; (11) Hα+[N II] map graciously provided by A. García-Barreto (García-Barreto et al. 1995); (12) Hα+[N II] map from Greenawalt et al. (1998); (13) Average extinction towards H II regions from Scoville et al. (2001); (14) Hα map graciously provided by S. Ryder via A. Vogler (Ryder et al. 1995); (15) Hα map from Larsen & Richtler (1999) (in NED); (16) Brα flux from Verma et al. (2003) in 14″×20″; (17) Brγ and Paβ fluxes from Dale et al. (2004) in ≈5″×5″ (most of starburst ring enclosed); (18) Brγ flux and extinction from Engelbracht et al. (1998); (19) Brγ flux from Stanford (1991) in 6″ × 8″; (20) Hα+[N II] map from Hibbard & van Gorkom (1996) (in NED); (21) Brγ flux and extinction from Krabbe et al. (1994); (22) Extinction and Q_Lyc from Förster Schreiber et al. (2001); (23) Brγ map provided by Böker (Böker et al. 1997); (24) Total Brγ flux from Moorwood & Oliva (1994); (25) Extinction from Brγ/Paβ of Doyon et al. (1994) in 3.5″ × 3.5″; (26) Brγ flux from Rieke et al. (1985) in 8.7″; (27) Paβ flux from Simpson et al. (1996) in a slit of width 1.5″; (28) Paα flux of the southern nucleus from Kawara et al. (1987); (29) Hα fluxes of both nuclei form Duc et al. (1997) in a slit of width 1.3″; (30) Brα flux from Sturm et al. (1996) in 14″ × 20″; (31) Brγ flux of Goldader et al. (1995) in a slit of width 0.75″.

† Values are for the GC extinction law of Lutz (1999a) when we made use of the Brα line at 4.05 μm (see Sect. 3.2).

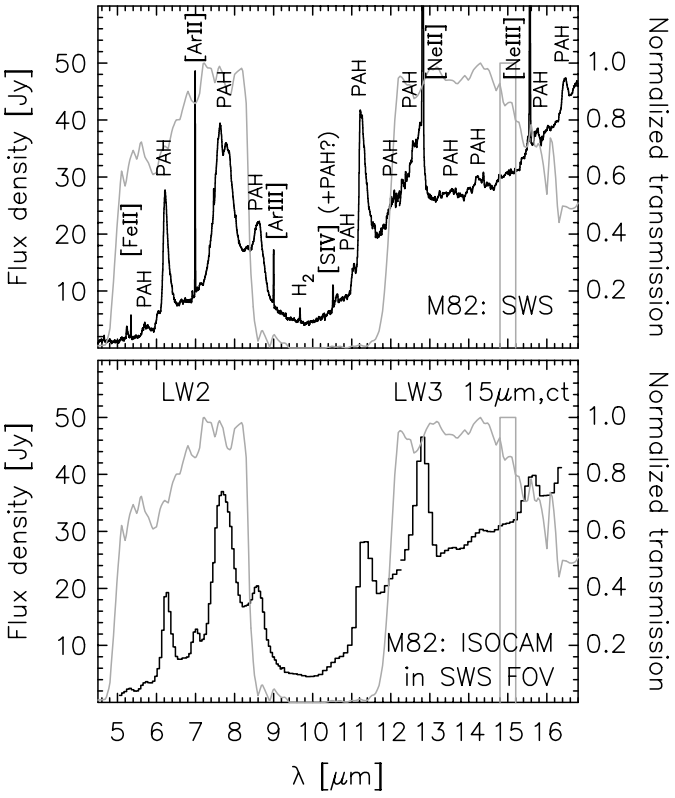

Fig. 1. Bandpasses of the MIR indicators of star formation activity. The transmission profiles of the ISOCAM *LW*2 and *LW*3 filters and the narrow band used for the monochromatic 15 μm,ct continuum measurements are shown by the grey lines. To illustrate the typical spectral features covered by these bandpasses, the spectra of the starburst galaxy M 82 obtained at $R \sim 500-1000$ with the ISO SWS and at $R \sim 40$ with ISOCAM within the SWS field of view are plotted in the top and bottom panels, respectively (from Förster Schreiber et al. 2001, 2003). Identifications of the emission features are labeled on the SWS spectrum.

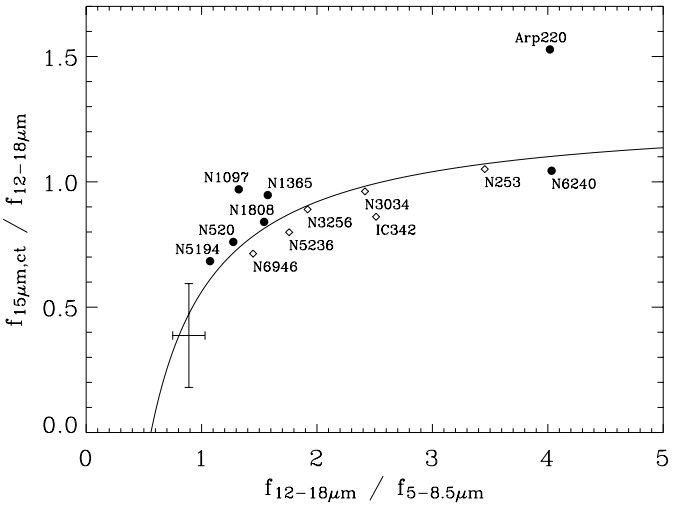

Fig. 2. Empirical relationship used to estimate the monochromatic 15 μm continuum flux density from broadband *LW*2 and *LW*3 measurements. The black circles represent circumnuclear regions of spiral galaxies and starburst systems for which both broadband and CVF data are available. Diamonds represent galaxies with only CVF data, for which broadband fluxes were synthesized from the spectrum. The line shows the least-squares fit obtained as explained in the text, $y = a - b/x$, where x and y are the abscissa and the ordinate. The error bar indicates the mean and 1σ dispersion in $f_{12-18\,\mu m}/f_{5-8.5\,\mu m}$ color of the sample of spiral disks, and the $f_{15\,\mu m,ct}/f_{12-18\,\mu m}$ ratio and measurement uncertainty for the disk of NGC 5236. The disk of this galaxy was chosen because its spectrum has the highest signal-to-noise ratio of the sample.

second component scaling linearly with the emission measured by $f_{15\,\mu m,\,ct}$, it is easy to show that $f_{15\,\mu m,\,ct}/f_{12-18\,\mu m}$ can be represented by an affine function of $1/(f_{12-18\,\mu m}/f_{5-8.5\,\mu m})$.

Excluding Arp 220, whose CVF spectrum suggests severe extinction effects, with high opacity from amorphous silicates at 9.7 μm and 18 μm (Rigopoulou et al. 1999), and NGC 1097 whose CVF spectrum is affected by residual memory effects, we used the least-squares fit to these data to assign a $f_{15\,\mu m,\,ct}/f_{12-18\,\mu m}$ ratio to the circumnuclear regions of spirals and starbursts without CVF data. Figure 2 shows also data for galaxies observed only in CVF mode, whose broadband fluxes were simulated from the spectrum (diamond symbols). Except for Arp 220 and NGC 1097, all data points are within 15% of the fitted relation. For spiral disks, we applied a uniform conversion justified by their small dispersion in $f_{12-18\,\mu m}/f_{5-8.5\,\mu m}$ (Roussel et al. 2001c; see also Dale et al. 2000, 2001). We used the ratio $f_{15\,\mu m,\,ct}/f_{12-18\,\mu m} = 0.38$ measured on the disk of NGC 5236 which has the best quality CVF spectrum among the disk sample.

We did not correct MIR flux densities for extinction. Relative to the optical V band (5500 Å), the extinction in magnitudes is very small, with $A_{5-8.5\,\mu m}/A_V$ and $A_{15\,\mu m}/A_V \leq 0.06$ (e.g. Draine 1989; Lutz 1999a). Extinction effects on the relationships studied in this work will be discussed in Sect. 4.

3.2. Star formation rate indicators: H recombination lines

To estimate SFRs, we used H recombination lines collected from the literature, which provide primary diagnostics and allowed us to derive the nebular extinction and correct for it. We converted all fluxes to a common reference quantity, the production rate of Lyman continuum photons Q_{Lyc}. We took care that consistent apertures were used to measure the dust and hydrogen line fluxes. Limitations of available data and the assumptions on physical conditions made in deriving Q_{Lyc} inevitably lead to appreciable uncertainties. We emphasize however that uncertainties for individual sources of even a factor two affect but little our conclusions, as will be discussed in Sect. 4.

For spiral disks, we used the total and circumnuclear Hα + [N II] $\lambda\lambda$6548, 6583 Å fluxes corrected for Galactic extinction listed by Roussel et al. (2001c) to obtain disk-only fluxes. We then derived intrinsic Hα fluxes following the precepts of Kennicutt (1983) applicable to H II regions in spiral disks, correcting for an average 25% contribution by the [N II] lines and an average internal extinction $A_{H\alpha} = 1.1$ mag (see also the discussion by Roussel et al. 2001c).

For the circumnuclear regions of spirals with two or more H line measurements, we derived the extinction by least-squares

fits to the ratios of observed fluxes to intrinsic line emissivities from Storey & Hummer (1995). We assigned equal weight to the ratios given the difficulty of determining the uncertainties for the inhomogeneous collection of H line data. We obtained the resulting $Q_{\rm Lyc}$ by averaging the individual $Q_{\rm Lyc}$ values derived from each dereddened line flux, taking the total H recombination coefficient from Storey & Hummer (1995). In some cases, relevant line data were not available or too uncertain, so we adopted published values of extinction insofar as determined from H lines. Since the extinction was sometimes derived in a region smaller than our photometric aperture, and the assumption of uniform extinction throughout kiloparsec scales is probably wrong, extinction corrections may introduce a non-negligible dispersion in the relations shown in Sect. 4.

Whenever circumnuclear Hα fluxes included the satellite [N II] lines, we applied the same correction factor of 0.75 as for the disks, the validity of which we verified as much as possible based on published spectroscopy from various sources. The compilations of Kennicutt et al. (1989), Kennicutt (1992) and Jansen et al. (2000) show that while there is significant overlap in [N II] λ6583 Å/Hα ratios between disk H II regions and nuclei of spiral galaxies, many (~50%) can exhibit much higher ratios, which can be explained by shock heating (e.g. by supernova remnants) or by a non-thermal Liner/Seyfert contribution. This line ratio increase is however observed in the immediate vicinity of nuclei; our circumnuclear regions are generally much larger so that this effect is not expected to be important.

We employed the extinction law of Cardelli et al. (1989) at $\lambda < 3\,\mu$m and of Lutz (1999a) at $\lambda \geq 3\,\mu$m. We adopted a uniform foreground screen model (UFS) for the geometry of the sources and obscuring dust. The limited number of H lines considered for each galaxy prevented us from constraining the extinction model, but computations for a homogeneous mixture of dust and sources ("MIX" model) imply $Q_{\rm Lyc}$ values differing by at most 56% (on average 18%) from those of the UFS model[3]. We assumed that the H II regions in all sample galaxies are ionization bounded, optically thick in the Lyman lines and optically thin in all others (case B recombination), and adopted electron density and temperature of $n_{\rm e} = 100\,{\rm cm}^{-3}$ and $T_{\rm e} = 5000$ K. These $n_{\rm e}$ and $T_{\rm e}$ were found representative for a sample of starbursts observed with SWS by Thornley et al. (2000), including most starbursts in our own ISOCAM sample. Higher values up to $n_{\rm e} = 10^4\,{\rm cm}^{-3}$ and $T_{\rm e} = 10^4$ K may be more appropriate for H II regions in normal spiral galaxies of near-solar metallicity (e.g. Smith 1975; Shaver et al. 1983; Giveon et al. 2002). However, the computations of Storey & Hummer (1995) imply variations of the relative emissivities of 13% on average (25% at most) for the lines considered here, little affecting the extinction estimates (<0.5 mag for the UFS model). The mean increase in the derived $Q_{\rm Lyc}$ between $n_{\rm e} = 100\,{\rm cm}^{-3}$, $T_{\rm e} = 5000$ K and $n_{\rm e} = 10^4\,{\rm cm}^{-3}$, $T_{\rm e} = 10^4$ K is 36% (maximum 55%), mainly driven by the variations of the total H recombination coefficient $\alpha_{\rm B}$ with $T_{\rm e}$ ($\alpha_{\rm B}$ depends only weakly on $n_{\rm e}$; Storey & Hummer 1995). In addition, we do not consider individual bright H II regions, but the total emission from large areas encompassing many star formation complexes. The average values of $n_{\rm e}$ and $T_{\rm e}$ are thus expected to be much lower than in resolved H II regions.

[3] The observed and intrinsic line fluxes F_λ and F^0_λ are related through $F_\lambda = F^0_\lambda\,{\rm e}^{-\tau_\lambda}$ for the UFS model and $F_\lambda = F^0_\lambda\,[(1-{\rm e}^{-\tau_\lambda})/\tau_\lambda]$ for the MIX model, where τ_λ is the optical depth of the obscuring material and the corresponding extinction in magnitudes is $A_\lambda = 1.086\,\tau_\lambda$.

3.3. Size normalization

To obtain scale- and distance-independent quantities, we normalized each measurement by the projected surface area and expressed the results in $L_\odot$ pc^{-2} (denoted hereafter $\Sigma_{5-8.5\,\mu{\rm m}}$, $\Sigma_{15\,\mu{\rm m,\,ct}}$, $\Sigma_{\rm Lyc}$). We chose these units specifically to avoid artificial correlation due to scale effects whereby the brighter (larger) galaxies tend to be brighter at all wavelengths. Normalizing all three quantities by the surface area eliminates dispersion from uncertainties in distance estimates. The $Q_{\rm Lyc}$ values were transformed into Lyman continuum luminosities $L_{\rm Lyc}$ assuming an average ionizing photon energy of 16 eV. We emphasize that although these quantities are formally equivalent to surface brightnesses, they are not intended as such and will be referred to as "size-normalized luminosities."

We normalized fluxes of spiral disks by the circular area of diameter D^B_{25}, the major axis length of the B-band isophote $\mu_B = 25$ mag arcsec^{-2} (from the RC3 catalog; de Vaucouleurs et al. 1991). This area encloses all detected MIR emission as defined by the $LW2$ isophote at 5 μJy arcsec^{-2}, the typical depth reached in these ISOCAM data, with isophote diameter ratios $D^{5-8.5\,\mu{\rm m}}_{5\,\mu{\rm Jy}}/D^B_{25}$ in the range 0.35−1, depending on the gas richness and inclination of galaxies (Roussel et al. 2001a). For galaxies with no available Hα map, it was verified that the aperture of the integrated Hα flux is larger than or comparable to the spatial extent of the MIR emission. The mismatch between the optical diameter and the actual sizes of the MIR and Hα emitting regions will introduce either a "correlation bias," whereby points move along a line of slope 1, or scatter in our relationships, depending on how well the MIR and Hα emission trace each other and are covered by the photometric apertures.

For the circumnuclear regions and starburst cores, we have striven to adopt as well a uniform and well-defined surface quantity. We extracted the size of the MIR source from azimuthally-averaged surface brightness profiles fitted with a Gaussian, after bringing all images to a common Gaussian PSF (see Appendix A). We chose a photometric aperture of 2.5 times the fitted half-power beam width (*HPBW*) in order to measure the total flux to a good aproximation; after deconvolution by the size of the PSF, the aperture is also used for area normalization. For the sources whose geometric structure is ill-suited to such a definition, we made exceptions explained in Appendix A. In particular, for the most compact sources (with respect to the ISOCAM angular resolution), NGC 4293, NGC 6240, IRAS 23128-5919 and Arp 220, we obtain in this way intrinsic sizes that are comparable to or smaller than the angular resolution, and therefore highly uncertain. Hence, for these galaxies, we did not use the fitted MIR sizes for area normalization, but starburst sizes derived from high-resolution observations in the literature.

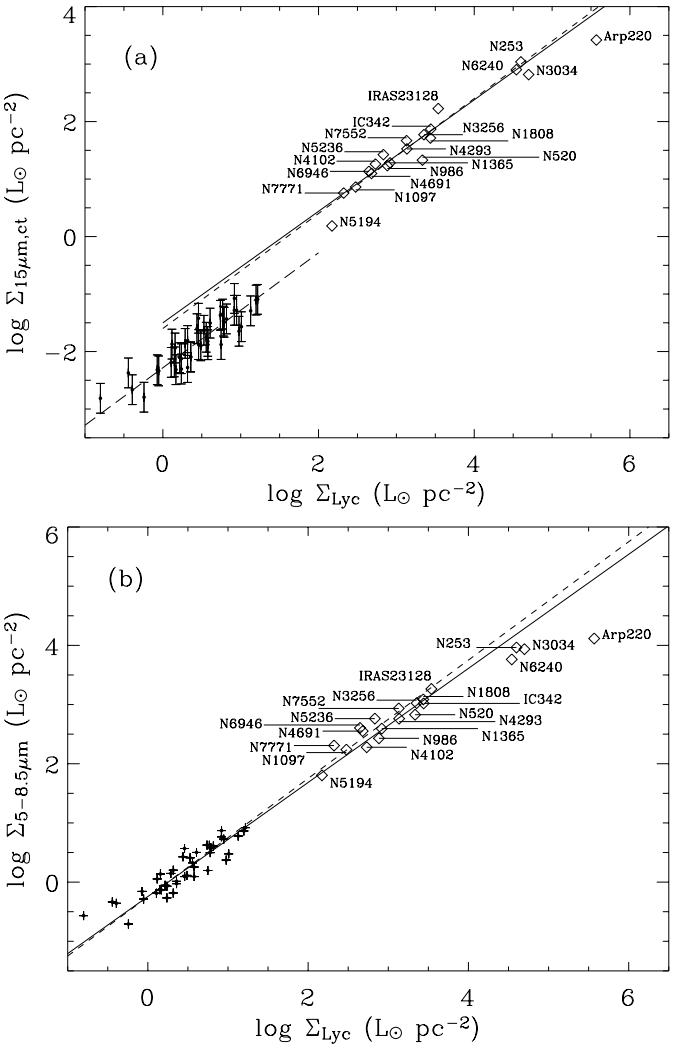

Fig. 3. Empirical relationships between the MIR dust emission and the Lyman continuum luminosity as a measure of the star formation rate. The quantities plotted are size-normalized luminosities, with different symbols used for the spiral disks (crosses), and the circumnuclear regions of spirals and starburst systems (diamonds). **a)** In the $\log(\Sigma_{15\,\mu\mathrm{m,ct}})-\log(\Sigma_{\mathrm{Lyc}})$ diagram, the solid line indicates the power-law least-squares fit performed on the circumnuclear regions and starbursts only, excluding the disks, NGC 5194 and Arp 220. The short-dashed line shows the fit result where the index was fixed to unity, and the long-dashed line shows a similar fit for disks alone. **b)** In the $\log(\Sigma_{7\,\mu\mathrm{m}})-\log(\Sigma_{\mathrm{Lyc}})$ diagram, the conventions are the same and fits were performed including the disks, but excluding NGC 253, NGC 3034 (=M 82), NGC 6240 and Arp 220.

4. Results

4.1. Calibration of MIR dust emission as star formation diagnostic

Figure 3 shows the relationships between the observed $\Sigma_{15\,\mu\mathrm{m,ct}}$ and $\Sigma_{7\,\mu\mathrm{m}}$ and the derived Σ_{Lyc} for our sample galaxies. The immediate result is that both MIR quantities constitute reliable SFR tracers over many orders of magnitude in Σ_{Lyc}. Thus, in a general sense, our results extend those previously found for spiral disks by Roussel et al. (2001c) and for NGC 253, NGC 1808, and M 82, including individual regions, by Förster Schreiber et al. (2003). Our enlarged sample reveals however interesting differences in the behaviour of the MIR tracers and between various source classes.

In the $\Sigma_{15\,\mu\mathrm{m,ct}}-\Sigma_{\mathrm{Lyc}}$ diagram, the monochromatic 15 μm continuum emission is directly proportional to the ionizing photon luminosity within the error bar on the power-law index, but with two different normalizations corresponding to two distinct regimes, each spanning 2–3 orders of magnitude in Σ_{Lyc}: 1) quiescent spiral disks, with low Lyman continuum luminosities per unit projected area $\Sigma_{\mathrm{Lyc}} \lesssim 10^2\ L_\odot\,\mathrm{pc}^{-2}$; and 2) moderately to actively star-forming regions in the central $\lesssim$1 kpc of spiral and starburst galaxies, with an activity level characterized by $\Sigma_{\mathrm{Lyc}} \gtrsim 10^2\ L_\odot\,\mathrm{pc}^{-2}$, but perhaps excluding extreme environments with $\Sigma_{\mathrm{Lyc}} \sim 10^5$–$10^6\ L_\odot\,\mathrm{pc}^{-2}$. Although the transition between the two regimes is certainly gradual, our data set includes but one object sampling it. It occurs approximately at the level of star formation activity seen in the inner $\approx$90″ plateau of M 51, which has a color $f_{12-18\,\mu\mathrm{m}}/f_{5-8.5\,\mu\mathrm{m}} \approx 1.1$. The offset between the normalization of disks and that of starbursts is nearly a factor 5, and cannot be caused by the different methods applied to estimate ionizing photon fluxes. Assuming direct proportionality in each separate regime, we obtain:

$$\log(\Sigma_{15\,\mu\mathrm{m,ct}}) = \log(\Sigma_{\mathrm{Lyc}}) - 2.28, \quad \log(\Sigma_{\mathrm{Lyc}}) < 2, \tag{1}$$

$$\log(\Sigma_{15\,\mu\mathrm{m,ct}}) = \log(\Sigma_{\mathrm{Lyc}}) - 1.60, \ 2 \le \log(\Sigma_{\mathrm{Lyc}}) < 5, \tag{2}$$

where all size-normalized luminosities are in $L_\odot\,\mathrm{pc}^{-2}$. The fits are shown as dashed lines in Fig. 3. The dispersions are, respectively, 0.22 dex for the disks (factor $\approx$1.6), and 0.18 dex for the galactic centers and starburst systems (factor 1.5), from which we have excluded NGC 5194 and Arp 220 at the extremes of the Σ_{Lyc} range. Linear least-squares fits, where the power-law index is let as a free parameter, yield an exponent of 1.01 ± 0.07 for disks and 0.97 ± 0.06 for starbursts.

The break between spiral disks and more active regions can be interpreted easily. In disks, the density of the radiation heating the dust is too low for the VSG continuum to be significant at 15 μm. In such conditions, the continuum starts rising at longer wavelengths where larger dust grains at lower temperatures re-emit the energy absorbed from the relatively diffuse radiation field. The emission detected at 15 μm is then dominated by PAHs or a related family of particles. Above a certain threshold in ionizing radiation density, VSG heating becomes more efficient such that the continuum starts to make a significant contribution at 15 μm, and another regime prevails. The break thus signals the onset of VSG emission at sufficient star formation densities. Since linear correlations represent adequately the data in both regimes, we infer that the respective contributions from each dust species vary almost linearly with Lyman continuum luminosity. The data of Arp 220 suggest a flattening of the relationship at the most extreme densities; its $\Sigma_{15\,\mu\mathrm{m,ct}}$ lies about a factor of 4 below a simple extrapolation of the linear correlation seen in the other starbursts and the circumnuclear regions. Since the MIR spectrum of Arp 220 shows some signs of high optical depth (Rigopoulou et al. 1999), this damping of the dust emission can easily be caused by extinction effects.

At 7 μm, the situation is much different. Perhaps surprisingly, the PAH emission remains as good a star formation

indicator in circumnuclear regions and starbursts as in spiral disks. The linear relationship previously defined by the disks alone holds up to $\Sigma_{\rm Lyc} \approx 10^4\ L_\odot\,{\rm pc}^{-2}$; adopting this value as transition point and assuming direct proportionality, we obtain:

$$\log(\Sigma_{7\,\mu{\rm m}}) = \log(\Sigma_{\rm Lyc}) - 0.25,\ 0 \le \log(\Sigma_{\rm Lyc}) < 4, \quad (3)$$

where again the size-normalized luminosities are in $L_\odot\,{\rm pc}^{-2}$. The dispersion of circumnuclear regions and starbursts is 0.17 dex when galaxies beyond $\Sigma_{\rm Lyc} = 10^4\ L_\odot\,{\rm pc}^{-2}$ are excluded, and increases to 0.25 dex (a factor 1.8) when the same objects as for the $\Sigma_{15\,\mu{\rm m,ct}}$–$\Sigma_{\rm Lyc}$ relation are considered. The dispersion of disks is 0.21 dex. Allowing the power-law index to vary, the least-squares fit over the entire $0 \le \Sigma_{\rm Lyc} < 4$ range gives an exponent of 0.96 ± 0.02.

The 7 μm fluxes start to deviate significantly from the extrapolation of the linear correlation defined by disks above $\Sigma_{\rm Lyc} \approx 10^4\ L_\odot\,{\rm pc}^{-2}$. The starburst cores of NGC 253, M 82 and NGC 6240 fall by a factor 2–3 below the expected values while Arp 220 lies more than an order of magnitude lower. Extinction effects alone cannot account for the saturation of the 7 μm emission beyond $\Sigma_{\rm Lyc} = 10^4\ L_\odot\,{\rm pc}^{-2}$, which is most probably caused by disappearance of the band carriers from the starburst cores (see Sect. 5). This is not in contradiction with the different relation found at 15 μm: the fact that VSGs are larger and more resilient than PAHs allows the 15 μm diagnostic to continue rising up to higher star-formation activity levels than the 7 μm emission, though eventually VSG destruction might become significant too.

Although extinction is not expected to be a dominant cause of the 7 μm emission deficit at high values of $\Sigma_{\rm Lyc}$, it could, however, increase the dispersion at the highest star formation rate densities, together with variations in the average physical conditions of the gas (electronic densities and temperatures) and in metallicity. Another, certainly more important source of scatter is due to limitations of the available H line measurements and data used to estimate the nebular extinction. In particular, although we tried to minimize such effects as much as possible, the apertures are not perfectly coincident, the angular resolutions are not perfectly matched, and the extinction correction was sometimes derived in a region much smaller than the aperture. In view of all the uncertainties arising from use of inhomogeneous data and from assumptions about physical conditions in H II regions, and considering the fact that the observed dispersions are very small compared to the dynamic range of our relations, we have demonstrated that the two dust tracers investigated here constitute satisfactory and quantitative star formation estimators. We insist that the galaxies included in our sample are all of near-solar metallicities, while the relation between ionizing photon luminosity and dust emission may be very sensitive to a decrease in carbon abundance.

4.2. MIR color as an indicator of compactness

Since the two dust tracers behave differently (the linearity ranges and dispersions of the relations discussed above are different), their variations relative to each other may provide useful diagnostics on the star formation activity. Figure 4 shows how the $L_{15\,\mu{\rm m,ct}}/L_{5-8.5\,\mu{\rm m}}$ ratio varies with increasing $\Sigma_{\rm Lyc}$. It

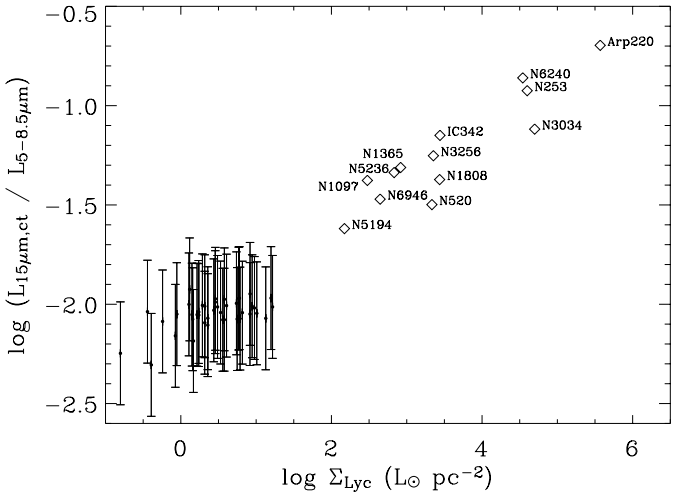

Fig. 4. Evolution of the $L_{15\,\mu{\rm m,ct}}/L_{5-8.5\,\mu{\rm m}}$ ratio with increasing Lyman continuum luminosity per unit projected surface area. Apart from the disks, only galaxies with a CVF spectrum are shown here.

should be noted here that the uncertainty on the actual size of the emitting regions, which affects only the abscissa, is potentially quite large. It is however expected to be at most a factor of a few, i.e. very small compared with the variation amplitude of $\Sigma_{\rm Lyc}$, which is three orders of magnitudes for the sole starburst regions. We find that the $\Sigma_{15\,\mu{\rm m,ct}}/\Sigma_{5-8.5\,\mu{\rm m}}$ ratio, tracing to the first order the ratio of VSG emission to PAH emission, increases regularly from disks to mild starbursts to extreme starbursts. A similar relationship was found by Dale et al. (2004) in nuclear regions and extranuclear H II regions of spiral galaxies. Their ionizing photon flux densities, derived in a uniform way from integral-field Paβ and Brγ lines, correspond to $\Sigma_{\rm Lyc}$, the quantity used here, between $10^{2.5}$ and $10^4\ L_\odot\,{\rm pc}^{-2}$. Although with a large dispersion, in part because of the inhomogeneous nature of the data used and the moderate angular resolution in the infrared, we show that this trend exists over a much larger range of star formation rate density.

$\Sigma_{\rm Lyc}$ is essentially a quantification of the compactness of star formation activity, and is affected both by geometry effects (filling factor of the interstellar medium by H II complexes) and by excitation effects (mass spectrum of ionizing stars). These two effects produce qualitatively similar results on the $\Sigma_{15\,\mu{\rm m,ct}}/\Sigma_{5-8.5\,\mu{\rm m}}$ ratio, the PAH emission being reduced because the sites of emission (mainly the surface of molecular clouds) collectively decrease in volume relative to H II regions, and because the PAH carriers may be destroyed over large spatial scales when the radiation field intensity becomes high enough. Excitation and density effects are intimately connected (Dale et al. 2004), but variations in radiation hardness (or age of the dominant stellar populations) are also expected to increase the color scatter, as was found by Roussel et al. (2001b) for central regions of spiral galaxies. The influence of metallicity differences is expected to be negligible for this particular sample, and differential extinction effects are very small compared with the dispersion, except perhaps for Arp 220.

5. Summary and conclusions

At mid-infrared wavelengths, dust species emitting aromatic bands seen mainly in the 6–13 μm range and a continuum rising toward longer wavelengths provide important observables for studies of star formation in dusty environments, and provide finer details than the far-infrared emission of grains in thermal equilibrium, because of much more favorable angular resolution and lesser source confusion. The fraction of the total infrared power produced by each of these two species is of the order of 10–20%, depending on the excitation conditions of dust grains (Dale et al. 2001; Dale & Helou 2002); the fraction contributed by very small grains, in particular, is remarkably constant up to very high average temperatures. In order for the SFR calibration at 5–8.5 μm derived here to be consistent with the calibration in terms of total infrared emission (between 8 and 1000 μm) proposed by Kennicutt (1998) for starbursts, the power emitted in the 5–8.5 μm range has to amount to 18% on average of the total infrared power (for galaxies less active than M 82). Owing to the fact that the far-infrared emission of galaxies is not spatially resolved by IRAS, and that the central regions selected here emit only a fraction of the integrated MIR emission of each galaxy, we cannot rigorously estimate the part of aromatic bands in the energy budget separately for disks and for galactic centers (but this will become feasible in local galaxies with observations by the Spitzer satellite). We only remark that a power fraction of 18% is somewhat larger than the fractions inferred by Dale et al. (2001) for a wide range of dust temperatures.

We have investigated the response of these dust species to the radiation field generated by massive stars, estimated independently and corrected for extinction, in a sample of star-forming sources of near-solar metallicity. In our sample, ionizing photon flux densities span a very wide range, from $\approx$1 to $\approx 10^{5.5}$ $L_\odot\,\mathrm{pc}^{-2}$. The regions considered here are spiral disks on one hand, representative of quiescent environments, and circumnuclear regions on the other hand, extended on spatial scales of the order of the kiloparsec.

Even though aromatic band carriers are on average heated by softer radiation than very small grains, we have shown that they can be used as a quantitative star formation tracer, their emission scaling linearly with the intrinsic emission of hydrogen recombination lines over a dynamic range of four orders of magnitude in ionizing photon flux densities. The relation found here confirms and extends that previously found for spiral disks up to much higher star formation rate densities. The global emission from aromatic bands starts to be damped past activity levels only just milder than that of M 82. By analogy with what is observed in and around H II regions in the Galaxy and the Magellanic Clouds, this saturation is most probably caused by the gradual destruction of aromatic band carriers effected by more and more intense far-ultraviolet radiation fields (Tran 1998; Contursi et al. 2000). In fact, this may be an indirect cause, Giard et al. (1994) having found a tighter relationship of the 3.3 μm PAH brightness with the ionized gas density than with the radiation field intensity. Additional agents of dust grain destruction may be found in the enhanced cosmic ray density from numerous supernova explosions (Mennella et al. 1997), and in high-velocity starburst winds (Normand et al. 1995).

Such a behavior as seen here in galaxies was previously reported for individual photodissociation regions by Boulanger et al. (1998). The approximate threshold at which they observe a significant depletion of aromatic bands is $\approx 10^{3.5}$ times the radiation field of the solar neighborhood G_0, or $10^{4.2}$ $L_\odot\,\mathrm{pc}^{-2}$ in the unit used here (adopting $G_0 = 2.2 \times 10^{-6}\,\mathrm{W\,m}^{-2}$ from Mathis et al. 1983). The threshold applicable to galactic starburst regions, occurring around $10^{4\pm0.5}$ $L_\odot\,\mathrm{pc}^{-2}$, is fully consistent with that found by Boulanger et al. (1998). It should be noted that resolution and dilution effects, as well as incomplete sampling of the explored radiation field range, hamper equally both studies, so that the actual value of the threshold is somewhat uncertain. The collective behavior of star-forming regions, integrated over kiloparsec scales, is nevertheless similar to that of individual H II regions and the associated neutral material surrounding them. This result suggests that the volume ratio of ionized regions on one hand, and surrounding regions where aromatic bands are excited on the other, does not vary in a systematic way up to the above mentioned radiation field intensity threshold, and then increases steadily, ionized regions occupying a growing fraction of the interstellar medium and starting to overlap.

The continuum of very small grains (sampled at 15 μm), on the other hand, provides a star formation rate tracer that is valid at higher radiation field intensities. In practice, variations of the spectral energy distribution of very small grains with their temperature distribution may cause appreciable deviations according to the sampled wavelength range, but we have shown here that the proportionality between ionizing photon fluxes and the 15 μm continuum is impressively tight, as soon as the VSG continuum dominates the bandpass, and at least up to $\Sigma_{\mathrm{Lyc}} = 10^5\,L_\odot\,\mathrm{pc}^{-2}$. Very small grains may also be destroyed in very harsh radiation fields (Contursi et al. 2000), but this effect is not observed here except possibly in Arp 220, where it is however not separable from optical depth effects.

New space missions such as Spitzer are making the mid-infrared window ever more accessible and are going to perform large surveys of galaxies. The choice to measure the continuum of very small grains at 15 μm was dictated by the limited wavelength coverage of the data we used. However, with the Spitzer satellite, this continuum will be observable primarily through the 20–28 μm filter of the MIPS instrument, and through the IRS Long-Low spectrometer for brighter galaxies. For local galaxies, these wavelengths promise an excellent star formation tracer, following a single regime from disk-like to very high radiation field intensities. The MIPS 24 μm filter will detect the continuum of very small grains from $z = 0$ to $z \approx 0.6$, shifting gradually down to 15 μm, then the aromatic band cluster at 6–9 μm at $z \approx 1.8$–2.7. The MIPS 70 μm filter will cover the continuum of very small grains from 30 μm to 15 μm from $z \approx 1.3$ to $z \approx 3.5$. The quantitative relationships that we have derived in this paper might thus prove very useful in the immediate future.

Acknowledgements. Our referee, Dr. D.A. Dale, is gratefully thanked for his swiftness and help in improving the dicussion flow. It is a

pleasure to thank all the persons who made some of the data used here available to us or publicly (and who are named in Table 3). V.C. would like to acknowledge the support of JPL contract 960803. This research made use of the NASA/IPAC Extragalactic Database (NED) which is operated by the Jet Propulsion Laboratory, California Institute of Technology, under contract with the National Aeronautics and Space Administration. The ISOCAM data presented in this paper were analyzed using and adapting the CIA package, a joint development by the ESA Astrophysics Division and the ISOCAM Consortium (led by the PI C. Cesarsky, Direction des Sciences de la Matière, CEA, France).

Appendix A: Notes on individual sources and photometry

We give here additional details concerning individual sources as well as MIR and line flux measurements, for the spiral galaxies whose circumnuclear regions are studied in this work and the starburst systems. Whenever the Hα data included a contribution by the adjacent [N II] $\lambda\lambda$ 6548, 6583 Å lines, we applied a correction factor of 0.75 to obtain pure Hα fluxes (see Sect. 3.2). "[N II]" refers to both lines at λ = 6548 and 6583 Å, except if the wavelength of the line actually meant is given. Unless explicitely specified otherwise, extinction values derived from H line measurements are referred to a uniform foreground screen (UFS) model, case B recombination, with n_e = 100 cm^{-3}, and T_e = 5000 K.

We brought the MIR maps in all bandpasses to the same angular resolution before performing aperture photometry, substituting the extended non-Gaussian PSF with a Gaussian PSF of *FWHM* 6″ (when the pixel size is 6″), 3.5″ (when the pixel size is 3″) or 3″ (when the pixel size is 1.5″). To do this, we used an iterative procedure with a gain of 5% to ensure convergence, centered on the brightest pixel at each step. When using a map to measure hydrogen recombination line fluxes, we then convolved this map to the same angular resolution as in the MIR. Except when contrary indication is given below, we chose an homogeneous definition of the aperture as 2.5 times the half-power beam width fitted on the central MIR brightness profiles; this provides a very good approximation of the total flux of the central regions, coinciding well with sizes reported in Roussel et al. (2001b) (obtained by decomposing brightness profiles into a Gaussian core and an exponential disk).

NGC 986 – We assumed that the extinction derived from the Hβ/Hα ratio in the central 4″ × 4″ from Véron-Cetty & Véron (1986) is representative of that in our larger aperture. The data of Véron-Cetty & Véron (1986) imply [N II] λ 6583 Å/(Hα + [N II] λ 6583 Å) = 0.30 at the nucleus.

NGC 1097 – This strongly barred Liner/Seyfert galaxy has a bright star-forming ring of diameter ≈20″ (e.g. Hummel et al. 1987; Kotilainen et al. 2000). The nucleus, which is resolved and separable from the ring in our maps, contributes negligibly to the integrated Hα and Brγ emission (Storchi-Bergman et al. 1996; Kotilainen et al. 2000), as well as to the total MIR emission. We used an aperture of 45″, encompassing the whole emission from the ring (Roussel et al. 2001b). We corrected for the average extinction based on the results of Kotilainen et al. (2000) derived from Hα/Brγ ratios. We recomputed the weighting by the Brγ luminosity, with adjustments for the [N II] contribution to their Hα data and the different extinction laws adopted.

NGC 1365 – We combined the Brγ measurement of Puxley et al. (1988) with the Hα flux integrated within the same region from an Hα + [N II] map to derive the extinction, and assumed that it represents accurately the extinction within our larger aperture. The Seyfert nucleus does not contribute importantly to the H line and MIR dust emission. The total Hα flux in the central 4″ × 4″ (Véron-Cetty & Véron 1986), which also includes emission from adjacent "hot spots," is only 8% of that in 40″. MIR diagnostic line ratios suggest that star formation activity dominates the low excitation (≤50 eV) line spectrum at these wavelengths as well as the MIR and far-infrared continuum luminosities (Sturm et al. 2002). The nucleus is unresolved in the ISOCAM maps, preventing an accurate estimate of its contribution to the MIR fluxes, but the ISOCAM CVF data do not provide evidence for a significant AGN contribution based on the diagnostics of Rigopoulou et al. (1999) and Laurent et al. (2000). The [N II]/(Hα + [N II]) ratio in the central 4″ × 4″ and in several hot spots within 14″ × 20″ is ≈0.3 (Alloin et al. 1981; Véron-Cetty & Véron 1986).

NGC 4102 – The nucleus is saturated in both ISOCAM *LW*2 and *LW*3 observations, more severely for *LW*2. This galaxy generates a powerful outflow detected in the Paβ and Brγ lines (Roussel et al. 2003).

NGC 4293 – Since the central MIR source is very small compared to the pixel size of the ISOCAM maps (Roussel et al. 2001a), we do not use the fitted aperture for area normalization, but instead the size derived from the Paα and Hα maps. The data of Véron-Cetty & Véron (1986) in the central 4″ × 4″ give a high line ratio [N II] λ 6583 Å/(Hα + [N II] λ 6583 Å) = 0.68 due to the Liner nucleus, and an Hα flux accounting for ≈9% of the flux in d = 32.4″.

NGC 4691 – We combined the Brγ measurement of Puxley et al. (1990) with the Hα flux integrated within the same region from an Hα + [N II] map to derive the extinction, and assumed that it remains the same within our larger aperture. The [N II]/(Hα + [N II]) ratio in the central hot spots is ≈0.3 (Keel 1983; García-Barreto et al. 1995, 1999). As the central structure contains multiple knots which are partly blended in the ISOCAM maps, and is not well represented by a single Gaussian (Roussel et al. 2001a), we strayed from our general definition to determine the area normalization. As the MIR and Hα emission of NGC 4691 lacks in the disk and is very diffuse outside the central star-forming knots, we simply selected pixels above the 3σ brightness level in the Hα map and added their areas to compute an equivalent diameter.

NGC 5194 – We considered the central emission plateau of diameter 90″. The motivation for this choice instead of selecting a smaller region around the nucleus was that the plateau represents a transition between disks and more active circumnuclear regions in terms of MIR properties. Besides, the emission from the Seyfert nucleus is diluted and completely negligible within this large aperture. We adopted the average extinction, weighted by intrinsic Hα luminosities, derived by Scoville et al. (2001) from Hα/Paα decrements of a large

sample of H II regions, assuming it is representative of the effective extinction throughout the central plateau. We applied a small correction to this extinction to account for the different line emissivities and extinction laws adopted. The [N II]/(Hα + [N II]) ratio in the central $d \lesssim 20''$ is high and reaches $\approx$0.85 due to the Seyfert nucleus but goes down to $\approx$0.3 outside these regions (Rose & Searle 1982).

NGC 5236 – Genzel et al. (1998) report in the SWS $14'' \times 20''$ aperture an extinction of 5 mag, larger than the value adopted here. The ratio [N II] λ6583 Å/(Hα + [N II] λ6583 Å) $\approx$0.3 in the central $\approx 5''$ (Keel 1984; Véron-Cetty & Véron 1986). The nucleus is saturated in the ISOCAM *LW*2 and *LW*3 maps, more severely for *LW*3. We thus used maps simulated from the CVF spectral cube to measure the *LW*2 and *LW*3 fluxes. We estimate in this way that the missing flux fractions due to saturation are 11% and 34% respectively, assuming that the effects discussed in Sect. 3.1, making photometry from CVFs uncertain by 10–20%, are negligible.

NGC 6946 – We combined the Brγ flux of Puxley et al. (1988) with the Hα flux integrated in the same aperture from an Hα + [N II] map. Keel (1984) gives [N II] λ6583 Å/(Hα + [N II] λ6583 Å) $\approx$ 0.37 in the central $8.1''$. We assumed the same ratio throughout our larger aperture to calibrate the Hα + [N II] map. The nucleus is saturated in the ISOCAM *LW*2 and *LW*3 maps, more severely for *LW*2. As for NGC 5236, we used maps simulated from the CVF spectral cube, and we estimate that the missing flux fractions due to saturation are 27% and 13%, respectively.

NGC 7552 – Verma et al. (2003) published Brα and Brβ fluxes obtained with SWS in a $14'' \times 20''$ aperture which matches fairly well our circular aperture of $21.8''$. We used Brα only because of possible blending of Brβ with H_2 1 − 0 O(2), and combined it with the Hα flux integrated over the same region from an Hα + [N II] map to derive the extinction. The nucleus is slightly saturated in the *LW*3 map. From the data of Véron-Cetty & Véron (1986) for the central $4'' \times 4''$, [N II] λ6583 Å/(Hα + [N II] λ6583 Å) = 0.37 and the Hα flux is 24% of the flux in $21.8''$.

NGC 7771 – Brγ and radio imaging shows that the central $d \approx 10''$ area hosts the active star-forming regions, distributed mainly along a circumnuclear ring (Neff & Hutchings 1992; Reunanen et al. 2000). Note that although Reunanen et al. (2000) mention that they corrected for velocity shifting of the Brγ line outside the narrow-band filter they used, the data from Dale et al. (2004), which we adopted, yield a Brγ flux almost three times higher in the central $5'' \times 10''$.

NGC 253 – The Seyfert nature of the nucleus (Véron-Cetty & Véron 2001) is unconfirmed by other optical spectroscopic studies, and by near- and mid-infrared spectroscopy (e.g. Engelbracht et al. 1998; Sturm et al. 2000); neither by our ISOCAM data based on the diagnostics of Rigopoulou et al. (1999) and Laurent et al. (2000). We used the Brγ flux of Engelbracht et al. (1998) integrated over $d = 15''$, which contains all the flux and coincides with the fitted size of the MIR emission. We used their Paβ/Brγ flux ratio measured in $2.4'' \times 12''$ to derive the extinction. Published extinction and $Q_{\rm Lyc}$ estimates from H line data vary greatly. For instance, Verma et al. (2003) derived from SWS line observations $A_{\rm V}^{\rm MIX} \sim 9$ mag, considerably lower than $A_{\rm V}^{\rm MIX} = 30$ mag reported by Genzel et al. (1998), although the $Q_{\rm Lyc}$ values are similar.

NGC 520 – Brγ line emission in this interacting system is detected at the primary nucleus within a region of $\sim 5'' \times 3''$ (Stanford 1991; Kotilainen et al. 2001). We combined the Brγ flux of Stanford (1991) in the central $6'' \times 8''$ with the Hα flux measured within the same aperture from an Hα+[N II] map, to derive the extinction. We made use of the Hα/(Hα+[N II]) ratio of 0.58 found by Veilleux et al. (1995) at the nucleus. Since the primary nucleus suffers from very large extinction, the use of Hα photometry in a larger aperture is especially uncertain.

NGC 1808 – We used the Brγ flux of Krabbe et al. (1994) integrated in a $20''$ aperture centered at the nucleus, which contains the quasi-totality of the flux and coincides reasonably well with the fitted MIR size. Krabbe et al. (1994) derived extinction values ranging from 3 to 5 mag from Hα/Brγ decrements, in excellent agreement with estimates from Hβ/Hα decrements quoted in the same paper, so we applied an average of 4 mag.

NGC 3034 (M 82) – We used directly the extinction and $Q_{\rm Lyc}$ results of Förster Schreiber et al. (2001) for the starburst core within $d = 30''$. These results were derived from an extensive set of H lines from optical to radio wavelengths which are best fitted by a mixed model and with deviations from the Draine (1989) extinction law, at $\lambda = 3{-}10\,\mu$m, as found towards the Galactic Center (Lutz 1999a). The MIR source is elongated along the optical major axis. Computing the quadratic mean of the major axis and minor axis widths, we find that $2.5 \times HPBW = 29.95''$ at 15 μm, thus extremely close to the adopted aperture of $30''$. The 5–8.5 μm emission is more extended, and we would have derived an aperture of $35''$ from it.

IC 342 – We adopted an aperture of $17'' \times 17''$ corresponding to the size of the Brγ line map provided by Böker et al. (1997), which encompasses the circumnuclear starburst ring. This aperture is close to the intrinsic size of the mid-IR source fitted on the surface brightness profiles, between $19''$ and $22''$. The areas agree to within 30%, and the MIR fluxes to within 9% in the different apertures. We combined the Brγ flux integrated over the map with the Brα flux of Verma et al. (2003) obtained in the $14'' \times 20''$ SWS beam (excluding their Brβ measurement because of possible contribution from the H_2 1−0 O(2) line and Pfα because of larger uncertainties on the extinction law near 7 μm). Fits assuming a UFS and a mixed model are both well constrained, and the derived extinctions imply nearly identical $Q_{\rm Lyc}$ (within 1%).

NGC 3256 – The MIR emission can be separated into two components of different sizes, a core of $\approx 8''$ superposed onto a source of $\approx 20''$. Therefore, a single Gaussian does not provide a good fit to the surface brightness profile. We adopt the size of the larger source as our aperture. Kawara et al. (1987) report a Brγ flux of 14.8×10^{-17} W m^{-2} in a smaller aperture of $9'' \times 18''$, almost identical to the total Brγ flux of 15×10^{-17} W m^{-2} measured by Moorwood & Oliva (1994) in a field of view of $34'' \times 34''$. We derive the extinction in the central $3.5'' \times 3.5''$ from the Paβ/Brγ ratio of Doyon et al. (1994) and assume that it does not vary inside our larger aperture.

NGC 6240 – The MIR emission of NGC 6240 is unresolved in the ISOCAM data. We adopt a size of 3″ based on the Brγ map of Tecza et al. (2000). As a comparison, we derive from brightness profile fitting a *HPBW* of the order of 2.7″, which is ill-constrained since it is smaller than the cleaned PSF *HPBW* of 3″. We adopted the Brγ flux of Rieke et al. (1985) measured in a 8.7″ aperture, and the Paβ flux of Simpson et al. (1996) measured in a slit of width 1.5″ oriented along the major axis of the source. In view of the Brγ map of Tecza et al. (2000), these apertures should include the total fluxes. The Paα flux of de Poy et al. (1986), measured in a 5.5″ aperture, yields a negative extinction when combined with the Paβ flux; it may thus be strongly underestimated. MIR diagnostics indicate that starburst activity dominates the dust emission and the low-excitation fine-structure line emission at these wavelengths (Genzel et al. 1998; Rigopoulou et al. 1999; Laurent et al. 2000; but see also Lutz et al. 2003).

IRAS 23128-5919 – The two galaxies in this merging pair are separated by a projected distance of less than 5″, and are marginally resolved by ISOCAM. We derive *HPBW*s of the order of 2.5″ for both nuclei. For lack of adequate high-resolution data, and in analogy with NGC 6240, we adopt a total size of 3″ for each nucleus, thus an equivalent size of 4.2″. To derive the extinction, we combined measurements of pure Hα and Paα fluxes in the southern nucleus, which is much brighter than the northern nucleus. Note that because of the narrow slit used by Duc et al. (1997), the Hα fluxes may be underestimated. In the MIR, we performed the brightness profile fitting and aperture photometry of the two blended nuclei together. Since the CVF spectrum has poor signal to noise ratio, and the 12–18 μm flux simulated from the CVF is not in agreement with the observed broadband flux, we used only broadband images. From both optical and MIR diagnostics, this system is classified as a starburst in which the large velocities observed in emission lines of the southern nucleus are caused by starburst superwinds (Johansson & Bergvall 1988; Lutz et al. 1999b).

Arp 220 – The two nuclei of this merger are separated by ≈1″ and are totally unresolved in the ISOCAM data. The size that we derive from 15 μm brightness profile fitting is 1.8–1.9″ *HPBW*. We use a total extent of 2″, as implied by the high angular resolution observations of the mid-IR emission by Soifer et al. (1999). MIR diagnostics indicate that starburst activity dominates the dust emission and the low-excitation fine-structure line emission (Genzel et al. 1998; Rigopoulou et al. 1999; Laurent et al. 2000; see also the detailed study by Spoon et al. 2003). The extinction that we derive from the Brα and Brγ fluxes is in good agreement with that predicted by Anantharamaiah et al. (2000) from a set of radio recombination lines.

Appendix B: Spectral observations of IC 342

The CVF observations of IC 342 consist of a single pointing centered on the nucleus, with the 3″ pixel^{-1} scale giving a 96″ × 96″ field of view, and contain ≈35 exposures of 2.1 s per wavelength channel for a total integration time of $3^{\rm h}\,18^{\rm m}$. A representative spectrum, in a region of 21″ × 21″, is shown in Fig. B.1. It shows all the usual features of star-forming galaxies, with aromatic bands nearly invariant in shape and relative intensity (see Fig. 1). Notice the faint emission bands that are also present in the spectra of the other galaxies of this sample, and which are attributable to carriers of the same nature as those emitting the bright bands at 6.2, 7.7, 8.6, 11.3 and 12.7 μm. Those contributing to the emission within the *LW*3 filter and observed in this spectrum are detected at 12.0, 13.6, 14.3 and 15.7 μm (Sturm et al. 2000).

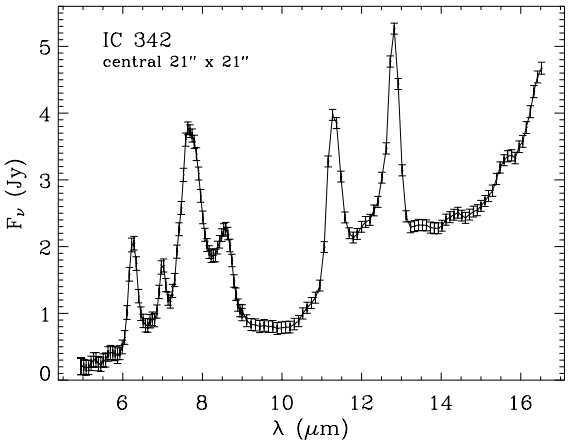

Fig. B.1. Mid-infrared spectrum of IC 342 summed over the central 21″ × 21″. The error bars represent the uncertainty on the subtracted zodiacal foreground. Errors arising from imperfect signal stabilization are not included, but are likely important at $\lambda \geq 15.5\,\mu$m.

References

Alloin, D., Edmunds, M. G., Lindblad, P. O., & Pagel, B. E. J. 1981, A&A, 101, 377
Anantharamaiah, K. R., Viallefond, F., Mohan, N. R., Goss, W. M., & Zhao, J. H. 2000, ApJ, 537, 613
Biviano, A., Altieri, B., Blommaert, J., et al. 1998a, The ISOCAM CVF Calibration Report, version 1.1, ESA/CAM IDT Vilspa Technical report
Biviano, A., Blommaert, J., Laurent, O., et al. 1998b, The ISOCAM Flat Field Calibration Report, version 1.1, ESA/CAM IDT Vilspa Technical report
Böker, T., Calzetti, D., Sparks, W., et al. 1999, ApJS, 124, 95
Böker, T., Förster Schreiber, N. M., & Genzel, R. 1997, AJ, 114, 1883
Boselli, A., Lequeux, J., Sauvage, M., et al. 1998, A&A, 335, 53
Boulanger, F., Abergel, A., Bernard, J. P., et al. 1998, ASP Conf. Ser., 132, 15
Cardelli, J. A., Clayton, G. C., & Mathis, J. S. 1989, ApJ, 345, 245
Cesarsky, C. J., Abergel, A., Agnèse, P., et al. 1996, A&A, 315, L32
Cesarsky, C. J., & Sauvage, M. 1999, Ap&SS, 269, 303
Charmandaris, V., Laurent, O., Le Floc'h, E., et al. 2002, A&A, 391, 429
Contursi, A., Lequeux, J., Cesarsky, C., et al. 2000, A&A, 362, 310
Coulais, A., & Abergel, A. 2000, A&AS, 141, 533
Crété, E., Giard, M., Joblin, C., et al. 1999, A&A, 352, 277
Dale, D. A., Helou, G., Contursi, A., Silbermann, N. A., & Kolhatkar, S. 2001, ApJ, 549, 215
Dale, D. A., & Helou, G. 2002, ApJ, 576, 159
Dale, D. A., Silbermann, N. A., Helou, G., et al. 2000, AJ, 120, 583
Dale, D. A., Roussel, H., Contursi A. et al., 2004, ApJ, 601, 813

Davidge, T. G., & Pritchet, C. J. 1990, AJ, 100, 102
de Graauw, T., Haser, L. N., Beintema, D. A., et al. 1996, A&A, 315, L49
de Poy, D. L., Becklin, E. E., & Wynn-Williams, C. G. 1986, ApJ, 307, 116
Désert, F. X., Boulanger, F., & Puget, J. L. 1990, A&A, 237, 215
de Vaucouleurs, G., de Vaucouleurs, A., Corwin, H. G., et al. 1991, Third Reference Catalog of Bright Galaxies (RC3)
Devereux, N. A., & Young, J. S. 1993, AJ, 106, 948
Doyon, R., Joseph, R. D., & Wright, G. S. 1994, ApJ, 421, 101
Draine, B. T. 1989, in Proc. of the 22nd ESLAB Symp., Infrared Spectroscopy in Astronomy, ed. B. H. Kaldeich, ESA SP-290, 93
Draine, B. T., & Anderson, N. 1985, ApJ, 292, 494
Duc, P.-A., Mirabel, I. F., & Maza, J. 1997, A&AS, 124, 533
Engelbracht, C. W., Rieke, M. J., Rieke, G. H., Kelly, D. M., & Achtermann, J. M. 1998, ApJ, 505, 639
Förster Schreiber, N. M., Genzel, R., Lutz, D., Kunze, D., & Sternberg, A. 2001, ApJ, 552, 544
Förster Schreiber, N. M., Sauvage, M., Charmandaris, V., et al. 2003, A&A, 399, 833
Freedman, W. L., & Madore, B. F. 1988, ApJ, 332, L63
García-Barreto, J. A., Aceves, H., Kuhn, O, et al. 1999, Rev. Mex. Astron. Astrofis., 35, 173
García-Barreto, J. A., Franco, J., Guichard, J., & Carrillo, R. 1995, ApJ, 451, 156
Geballe, T. R. 1997, in From Stardust to Planetesimals, ed. Y. J. Pendleton & A. G. G. M. Tielens (San Francisco: ASP), ASP Conf. Ser., 122, 119
Genzel, R., & Cesarsky, C. J. 2000, ARA&A, 38, 761
Genzel, R., Lutz, D., Strum, E., et al. 1998, ApJ, 498, 579
Giard, M., Bernard, J. P., Lacombe, F., Normand, P., & Rouan, D. 1994, A&A, 291, 239
Giveon, U., Sternberg, A., Lutz, D., Feuchtgruber, H., & Pauldrach, A. W. A. 2002, ApJ, 566, 880
Goldader, J. D., Joseph, R. D., Doyon, R., & Sanders, D. B. 1995, ApJ, 444, 97
Greenawalt, B., Walterbos, R. A. M., Thilker, D., et al. 1998, ApJ, 506, 135
Greenberg, J. M. & Hong, S.-S. 1974, IAUS, 60, 155
Hameed, S., & Devereux, N. A. 1999, AJ, 118, 730
Helou, G. 1986, ApJ, 311, L33
Helou, G., Lu, N. Y., Werner, M. W., Malhotra, A., & Silbermann, N. 2000, ApJ, 532, L21
Hibbard, J. E., & van Gorkom, J. H. 1996, AJ, 111, 655
Hony, S., Van Kerckhoven, C., Peeters, E., et al. 2001, A&A, 370, 1030
Hummel, E., van der Hulst, J. M., & Keel, W. C. 1987, A&A, 172, 32
Jansen, R.A., Fabricant, D., Franx, M., & Caldwell, N. 2000, ApJS, 126, 331
Johansson, L., & Bergvall, N. 1988, A&A, 192, 81
Kawara, K., Nishida, M., & Gregory, B. 1987, ApJ, 321, L35
Keel, W. C. 1983, ApJS, 52, 229
Keel, W. C. 1984, ApJ, 282, 75
Kennicutt, R. C., Jr. 1983, ApJ, 272, 54
Kennicutt, R. C., Jr. 1992, ApJ, 388, 310
Kennicutt, R. C., Jr. 1998, ARA&A, 36, 189
Kennicutt, R. C., Jr., Keel, W. C., & Blaha, C. A. 1989, AJ, 97, 1022
Kessler, M. F., Steinz, J. A., Anderegg, M. E., et al. 1996, A&A, 315, L27
Kewley, L. J., Heisler, C. A., Dopita, M. A., & Lumsden, S. 2001, ApJS, 132, 37
Kim, D.-C., Veilleux, S., & Sanders, D. B. 1998, ApJ, 508, 627
Koopmann, R. A., Kenney, J. D. P., & Young, J. S. 2001, ApJS, 135, 125
Kotilainen, J. K., Reunanen, J., Laine, S., & Ryder, S. D. 2000, A&A, 353, 834
Kotilainen, J. K., Reunanen, J., Laine, S., & Ryder, S. D. 2001, A&A, 366, 439
Krabbe, A., Sternberg, A., & Genzel, R. 1994, ApJ, 425, 72
Kristen, H., Jörsäter, S., Lindblad, P. O., & Boksenberg, A. 1997, A&A, 328, 483
Larsen, S. S., & Richtler, T. 1999, A&A, 345, 59
Laurent, O., 1999, Ph.D. Thesis, Université de Paris XI
Laurent, O., Mirabel, I. F., Charmandaris, V., et al. 2000, A&A, 359, 887
Léger, A., & Puget, J. L. 1984, A&A, 135, L5
Li, A., & Draine, B. T. 2002, ApJ, 572, 232
Lindblad, P. O. 1999, A&ARv., 9, 221
Lu, N., Helou, G., Werner, M.W., et al. 2003, ApJ, 588, 199
Lutz, D. 1999a, in The Universe as seen by *ISO*, ed. P. Cox & M. F. Kessler (Noordwijk: ESA), ESA SP-427, 623
Lutz, D., Veilleux, S., & Genzel, R. 1999b, ApJ, 517, L13
Lutz, D., Sturm, E., Genzel, R., et al. 2003, A&A, 409, 867
Malhotra, S., Helou, G., van Buren, D., et al. 1996, A&A, 315, L161
Mathis, J. S., Mezger, P. G., & Panagia, N. 1983, A&A, 128, 212
Mattila, K., Lemke, D., Haikala, L. K., et al. 1996, A&A, 315, L353
Mattila, K., Lehtinen, K., & Lemke, D. 1999, A&A, 342, 643
Mennella, V., Baratta, G. A., Colangeli, L., et al. 1997, ApJ, 481, 545
Mirabel, I. F., Vigroux, L., Charmandaris, V., et al. 1998, A&A, 333, L1
Moorwood, A. F. M., & Oliva, E. 1994, ApJ, 429, 602
Neff, S. G., & Hutchings, J. B. 1992, AJ, 103, 1746
Normand, P., Rouan, D., Lacombe, F., & Tiphène, D. 1995, A&A, 297, 311
Okumura, K. 2000, in *ISO* Beyond Point Sources: Studies of Extended Infrared Emission, ed. R. J. Laureijs, K. Leech, & M. F. Kessler, ESA SP-455, 47
Peeters, E., Hony, S., van Kerckhoven, C., et al. 2002, A&A, 390, 1089
Puget, J. L., & Léger, A. 1989, ARA&A, 27, 161
Puxley, P. J., Hawarden, T. G., & Mountain, C. M. 1988, MNRAS, 234, SC29
Puxley, P. J., Hawarden, T. G., & Mountain, C. M. 1990, ApJ, 364, 77
Reunanen, J., Kotilainen, J. K., Laine, S., & Ryder, S. D. 2000, ApJ, 529, 853
Rieke, G. H., Cutri, R. M., Black, J. H., et al. 1985, ApJ, 290, 116
Rigopoulou, D., Spoon, H. W. W., Genzel, R., et al. 1999, AJ, 118, 2625
Rose, J. A., & Searle, L. 1982, ApJ, 253, 556
Roussel, H., Vigroux, L., Bosma, A., et al. 2001a, A&A, 369, 473
Roussel, H., Sauvage, M., Vigroux, L., et al. 2001b, A&A, 372, 406
Roussel, H., Sauvage, M., Vigroux, L., & Bosma, A. 2001c, A&A, 372, 427
Roussel, H., Helou, G., Beck, R., et al. 2003, ApJ, 593, 733
Ryder, S. D., Hungerford, A., Dopita, M. A., et al. 1995, in The Opacity of Spiral Disks, ed. J. I. Davies & D. Burstein (Dordrecht: Kluwer), 359
Saha, A., Claver, J., & Hoessel, J. G. 2002, AJ, 124, 839
Sanders, D. B., & Mirabel, I. F. 1996, ARA&A, 34, 749
Sauvage, M., Blommaert, J., Boulanger, F., et al. 1996, A&A, 315, L89
Sauvage, M., & Thuan, T.X. 1992, ApJ, 396, L69
Scoville, N. Z., Polletta, M., Ewald, S., et al. 2001, AJ, 122, 3017
Sellgren, K., Luan, L., & Werner, M. W. 1990, ApJ, 359, 384

Shaver, P. A., McGee, R. X., Newton, L. M., Danks, A. C., & Pottasch, S. R. 1983, MNRAS, 204, 53
Simpson, C., Forbes, D. A., Baker, A. C., & Ward, M. J. 1996, MNRAS, 283, 777
Smith, H. E. 1975, ApJ, 199, 591
Soifer, B. T., Neugebauer, G., Matthews, K., et al. 1999, ApJ, 513, 207
Spoon, H. W., Moorwood, A. F., Lutz, D., et al. 2003 [arXiv:astro-ph/0310721]
Stanford, S. A. 1991, ApJ, 381, 409
Storchi-Bergman, T., Wilson, A. S., & Baldwin, J. A. 1996, ApJ, 460, 252
Storey, P. J., & Hummer, D. G. 1995, MNRAS, 272, 41
Sturm, E., Lutz, D., Genzel, R., et al. 1996, A&A, 315, L133
Sturm, E., Lutz, D., Tran, D., et al. 2000, A&A, 358, 481
Sturm, E., Lutz, D., Verma, A., et al. 2002, A&A, 393, 821
Tecza, M., Genzel, R., Tacconi, L. J., et al. 2000, ApJ, 537, 178
Thornley, M. D., Förster Schreiber, N. M., Lutz, D., et al. 2000, ApJ, 539, 641
Tokunaga, A. 1997, in Diffuse Infrared Radiation and the *IRTS*, ed. H. Okuda, T. Matsumoto, & T. L. Roellig (San Francisco: ASP), ASP Conf. Ser., 124, 149
Tran Q. D., 1998, Ph.D. Thesis, Université de Paris XI
Tran, Q. D., Lutz, D., Genzel, R., et al. 2001, ApJ, 552, 527
Tully, R. B. 1988, Nearby Galaxies Catalog (Cambridge University Press)
Uchida, K. I., Sellgren, K., & Werner, M. W. 1998, ApJ, 493, L108
Uchida, K. I., Sellgren, K., Werner, M. W., & Houdashelt, M. L. 2000, ApJ, 530, 817
Veilleux, S., Kim, D.-C., Sanders, D. B., Mazzarella, J. M., & Soifer, B. T. 1995, ApJS, 98, 171
Verma, A., Lutz, D., Sturm, E., et al. 2003, A&A, 403, 829
Véron-Cetty, M.-P., & Véron, P. 1986, A&AS, 66, 335
Véron-Cetty, M.-P., & Véron, P. 2001, A&A, 374, 92
Verstraete, L., Puget, J.-L., Falgarone, E., et al. 1996, A&A, 315, L337